PCCP

Elucidating the optical spectra of $[Au_{25}(SR)_{18}]^q$ nanoclusters

Journal:	*Physical Chemistry Chemical Physics*
Manuscript ID	CP-ART-07-2019-003982.R1
Article Type:	Paper
Date Submitted by the Author:	14-Sep-2019
Complete List of Authors:	Juarez-Mosqueda, Rosalba; University of Pittsburgh, Chemical and Petroleum Engineering Mpourmpakis, Giannis; University of Pittsburgh, Chemical and Petroleum Engineering

SCHOLARONE™
Manuscripts

Elucidating the optical spectra of $[Au_{25}(SR)_{18}]^q$ nanoclusters

Rosalba Juarez-Mosqueda [1] and Giannis Mpourmpakis [1,a]

[1]Department of Chemical Engineering, University of Pittsburgh, Pittsburgh, PA 15261, USA.

[a]e-mail:gmpourmp@pitt.edu

Abstract: Ligand-protected Au nanoclusters have attracted tremendous interest due to their atomically precise structural determination and controllable optical properties. However, the origin of their optical features is not well understood. Herein, we address the effects of charge state and type of ligands on the structural, electronic, and optical properties of the $Au_{25}(SR)_{18}$ nanocluster, using first principles calculations. In particular, we analyze in detail the optical absorption spectra of phenylethanethiol-capped $[Au_{25}(SCH_2CH_2Ph)_{18}]^q$ nanocluster (q= 1-, 0, and 1) and demonstrate that the nanocluster undergoes geometric changes when increasing its charge state, yielding the development of additional photoabsorption features. Moreover, by comparing the properties of the anionic $[Au_{25}(SR)_{18}]^{1-}$ nanoclusters (with SR= $-SCH_2CH_2Ph$, $-SCH_3$ and -SH) we demonstrate that accounting for full ($-SCH_2CH_2Ph$) compared to simplified ($-SCH_3$ and -SH) ligands leads to significant modifications in the shape of the main absorption features, such as the emergence of step-like absorption shoulders. In addition, we show that the energy of the main absorption peaks of the $[Au_{25}(SR)_{18}]^{1-}$ significantly blue-shifts when using -SH as model ligands. Overall, our computational work aids the experimental characterization of optical properties of ligand-protected nanoclusters and highlights the importance of accounting for full ligands in optical spectra calculations.

Introduction

Since the pioneering X-ray structure determination of $Au_{102}(p\text{-}MBA)_{44}$ in 2007, over a hundred of atomically precise ligand-protected nanoclusters have been successfully characterized from X-ray crystallography[1-3], opening great avenues in other research areas such as computations[4-6] and catalysis[7]. This includes the thiolate-protected $Au_{25}(SR)_{18}$ nanocluster, the crystal structure of which was determined for the first time in 2008[5, 8, 9]. To date, due to the synthetic accessibility of monodispersed $Au_{25}(SR)_{18}$ nanocrystals, this nanocluster is the most thoroughly investigated member of the growing family of ligand-protected nanoclusters[5, 10, 11].

In its native form, the $Au_{25}(SR)_{18}$ nanocluster is negatively charged and its electroneutrality is granted by the presence of a counterion (e.g. the Oct_4N^+ cation). As anion, the $[Au_{25}(SR)_{18}]^{1-}$ nanocluster exhibits a remarkable electronic stability characterized by a large HOMO-LUMO band gap (E_g). According to the superatom model[12] and the electron count formula introduced by

Häkkinen *et al*.[13], the electronic stability of $[Au_{25}(SR)_{18}]^{1-}$ was attributed to an eight-electron shell closure of delocalized Au(6s) electrons[12, 13]. Despite its electronic stability, the anionic $[Au_{25}(SR)_{18}]^{1-}$ cluster undergoes electron loss when exposed to moderated oxidizing conditions (such as in the presence of oxygen or mild chemical oxidants), which results in the formation of stable $[Au_{25}(SR)_{18}]^{0}$ and $[Au_{25}(SR)_{18}]^{1+}$ species [14-17]. The first report regarding the conversion of $[Au_{25}(SR)_{18}]^{1-}$ into a neutral cluster was published by Zhu *et al*[14]. The authors observed that, upon exposure to air for several hours, the anionic nanocluster spontaneously oxidizes undergoing noticeable changes in its inorganic core and absorption optical spectra. In particular, the authors found that the absorption spectrum of the oxidized $[Au_{25}(SR)_{18}]^{0}$ cluster develops an additional absorption shoulder at 630 nm (≈2.0 eV) and that the intensity of the characteristic peak at 450 nm (≈2.7 eV) decreases. To date, these distinct features in the spectrum of $[Au_{25}(SR)_{18}]^{0}$ have been observed in several spectroscopic experiments and theoretical studies[14, 16, 18, 19]. Despite this, the origin of these distinctive absorption features developed in the spectrum of the oxidized clusters has not yet been investigated in depth.

On the other hand, the absorption spectra of the anionic $[Au_{25}(SR)_{18}]^{1-}$ nanocluster have been extensively studied, both experimentally and theoretically.[9, 17, 20-22] Over the last decade, several computational studies have focused on understanding the spectral features and excited state properties of the $[Au_{25}(SR)_{18}]^{1-}$ nanocluster[9, 16, 21-27]. The great majority of these studies, however, has been performed using simplified structures in which the -SR group (which typically is -SCH_2CH_2Ph, -SC_6H_{13}, -SG (HSG = glutathione), -SPh, and para-substituted -SPhX[28-30]) is replaced by -SH, -SCH_3, -SCH_2CH_3, or -$SCH_2CH_2CH_3$[9, 21, 23-27] ligands. Typically the use of the simplified nanoclusters to reduce computational cost can be justified by the fact that the major physicochemical properties of these nanoclusters are mainly determined by the energy and electronic configuration of the frontier molecular orbitals as per the spherical superatom model[13]. However, it is known that the choice of the ligands can play an important role in determining the shape and energy of the spectral features, including absorption peaks that are mainly determined by metal-to-metal electronic transitions[24, 31]. Thus, several computational studies in which the -SCH_3 or -SH are used as simplified ligands to simulate the absorption spectra of $[Au_{25}(SR)_{18}]^{1-}$ may have missed fine spectral features that are caused by ligand-field effects[9, 23, 25]. In addition, although the spectrum of $[Au_{25}(SCH_2CH_2Ph)_{18}]^{1-}$ has been computationally determined, the characterization of the main absorption peaks is still missing. Therefore, calculating the electronic transitions of the $[Au_{25}(SR)_{18}]^{1-}$ using the actual (experimentally used) ligands is essential to facilitate the assignment of electronic transitions in the experimental spectrum, address ligand effects, and improve the agreement between experiments and theory.

Towards this aim, in this work we performed density functional theory (DFT) and time-dependent DFT (TDDFT) calculations using the phenylethanethiolate-protected crystal structures, $[Au_{25}(SCH_2CH_2Ph)_{18}]^{1-}$, and the simplified models, $[Au_{25}(SCH_3)_{18}]^{1-}$ and $[Au_{25}(SH)_{18}]^{1-}$. We compare the absorption spectra and ground state properties of these three structures with the aim of accounting for ligand effects. Our results demonstrate that the actual -SCH_2CH_2Ph ligands

introduce small distortions in the metal core that yield to significant modifications in the shape of the absorption spectrum of the anionic cluster (compared to simplified ligands). Moreover, the absorption energy of the main peaks can be significantly blue-shifted when using –SH as model ligands. Moreover, we analyzed in detail the absorption spectra of the $[Au_{25}(SCH_2CH_2Ph)_{18}]^q$ nanoclusters (q= -1, 0, and 1) to determine the effect of the charge state on photoabsorption. We found that distortions of the metal core become more pronounced when the charge state of the nanocluster increases (*i.e.* going from the anionic, to neutral, to cationic cluster) resulting in three distinct absorption spectra.

Computational methods

The electronic structure calculations were carried out within the framework of density functional theory (DFT) and time-dependent DFT (TDDFT) using the Perdrew-Burke-Ernzerhof (PBE) functional[32]. The absorption spectra of the $[Au_{25}(SR)_{18}]^q$ nanoclusters were calculated using linear response TDDFT based on Casida approach. All the calculations were performed in the computational code GPAW[20, 33] using the real-space multigrid method with uniform spacing of 0.2 Å. The crystal structure of $[Au_{25}(SCH_2CH_2Ph)_{18}]^{1-}$ was obtained from literature[8], and used as initial geometry for the optimizations of the anionic, neutral, and cationic $[Au_{25}(SR)_{18}]^q$ nanoclusters. The atomic charges were analyzed based on the Bader method[34].

Results and discussion

In Figure 1, we show the crystal structures of the $[Au_{25}(SCH_2CH_2Ph)_{18}]^q$ nanoclusters. In general, the structure of these nanoclusters consist of central Au atom surrounded by a Au_{12} core (forming together an icosahedral Au_{13} kernel), and six staple-like -SR-Au-SR-Au-SR- units. In these nanoclusters there are three different types of Au atoms: 1) a central Au atom whose coordination number is 12 (*i.e.* one bond with each of the 12 Au atoms of the Au_{12} core, Au_{center}-Au_{core}); 2) twelve Au atoms forming the vertices of the icosahedral structure, whose coordination number is 6 (each of these Au atoms forms 5 bonds with the neighboring Au atoms within the Au_{12} core, Au_{core}-$Au_{core,}$ and one bond with a S atom of the units, Au_{core}-S); and 3) twelve Au atoms forming the six $Au_2(SR)_3$ units (each of these Au atoms forms two Au_{units}-S bonds). The different types of bonding formed by the distinct Au atoms are shown in Figure 1B.

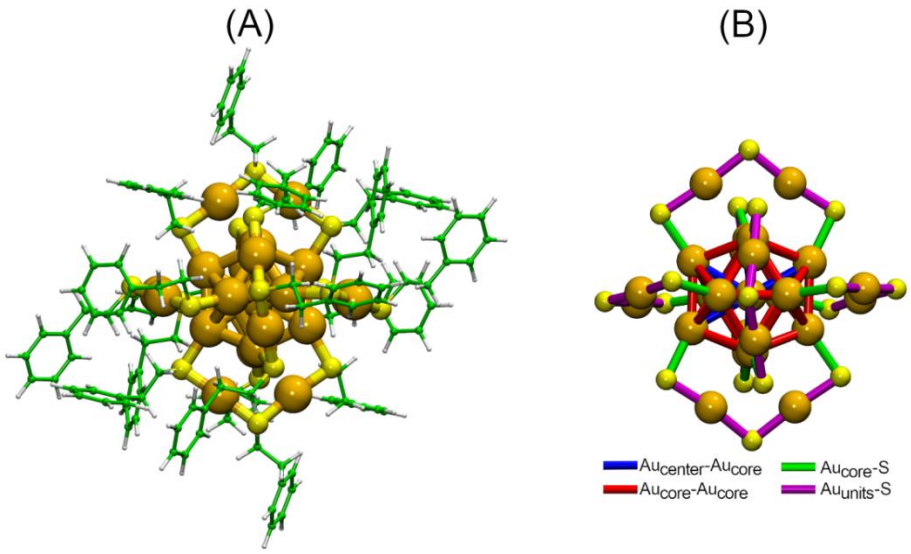

Figure 1. Atomic structure of the (A) $[Au_{25}(SCH_2CH_2Ph)_{18}]^q$ nanoclusters and (B) the representation of the $Au_{25}S_{18}$ inorganic core. The different types of bonds within the $Au_{25}S_{18}$ core are shown in (B) with different colors: bonds between the central Au atom and Au atoms of the Au_{12} core (Au_{center}-Au_{core}) are in blue; bonds between the Au atoms within the core (Au_{core}-Au_{core}) are in red; bonds between the Au atoms of the Au_{12} core and the S atoms (Au_{core}-S) are in green; bonds between Au and S atoms within the units (Au_{units}-S) are in magenta. Orange, yellow, green, and white spheres represent the Au, S, C, and H atoms.

Using the optimized $[Au_{25}(SCH_2CH_2Ph)_{18}]^q$ nanoclusters (q = -1, 0, and 1), we analyzed the changes in the bond lengths of Au_{center}-Au_{core}, Au_{core}-Au_{core}, Au_{core}-S, and Au_{units}-S due to cluster oxidation (see Figure 2). Comparing the three nanoclusters, we found that the Au_{center}-Au_{core} and Au_{core}-Au_{core} bonds of the Au_{13} kernel elongate significantly as the nanocluster charge state increases (*i.e.* going from the negative, to neutral, to positive, respectively). In particular, with respect to the anionic nanocluster, the length of the Au_{core}-Au_{core} bonds in the neutral and cationic clusters increases by up to ≈ 0.16 Å (5%) and ≈ 0.41 Å (14%), respectively. Also, the Au_{core}-S bonds slightly shrink (by less than 2%) as the charge state of the cluster increases. The Au_{units}-S bonds, on the other hand, remain unaffected by the nanocluster charge state (see individual and averaged values of bond distances in Table S1 of the supporting information file). In the first report on the conversion of $[Au_{25}(SCH_2CH_2Ph)_{18}]^{1-}$ into a charge neutral cluster, the authors indicated that structural distortions were observed in the structure of the anionic nanocluster, but not in the neutral cluster[14]. However, theoretical studies suggested that the apparent distortions of the anionic structure may be due to the presence of the Oct_4N^+counterion[35].Thus, in accordance with other computational studies[16], our results demonstrate that the distortions in the $Au_{25}S_{18}$ core become more significant as the charge state of the clusters increases.

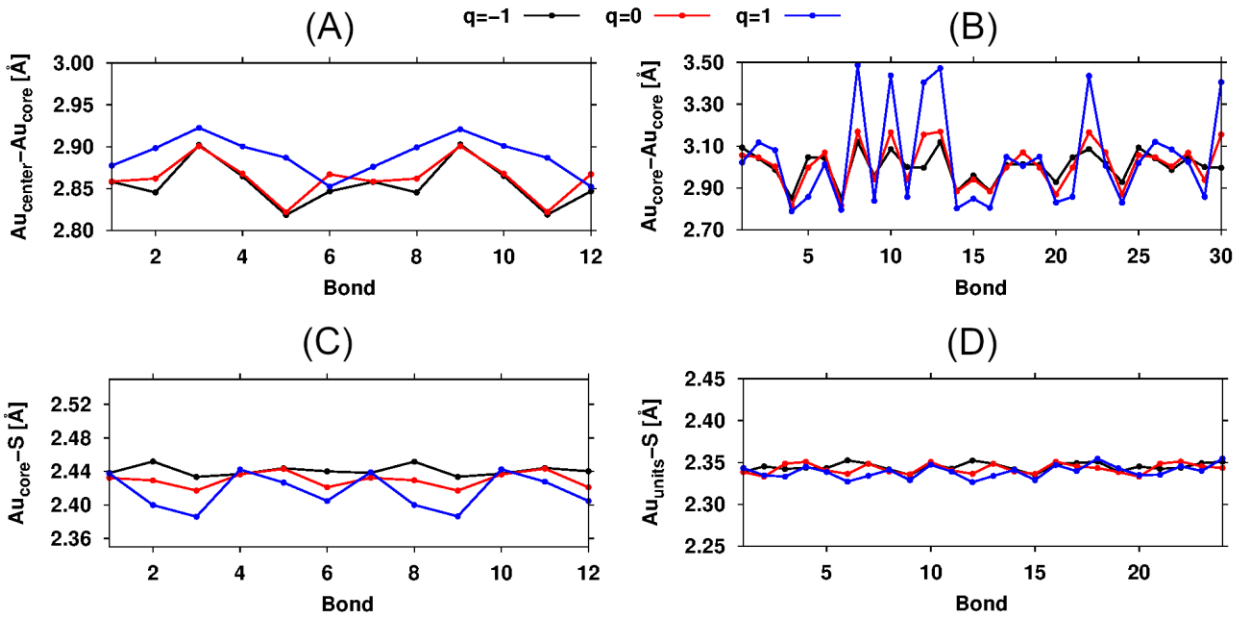

Figure 2. Individual (A) Au_{center}-Au_{core}, (B) Au_{core}-Au_{core}, (C) Au_{core}-S, and (D) Au_{units}-S bond distances of the $[Au_{25}(SCH_2CH_2Ph)_{18}]^{1-}$ (black), $[Au_{25}(SCH_2CH_2Ph)_{18}]^{0}$ (red), and $[Au_{25}(SCH_2CH_2Ph)_{18}]^{1+}$ (blue) nanoclusters.

Furthermore, we analyzed the changes in the atomic charges of the Au and S atoms when going from the anionic, to neutral, to positively charged nanoclusters, based on Bader analysis[34]. As shown in Figure 3A, we found that the charge of the Au atoms of the metal core systematically increases as the nanocluster oxidation state increases. Interestingly we found that the S atoms involved in the shortest Au_{core}-S bonds (Figure 2C) show the most negative atomic charges (see Figure 3B), thus correlating geometric distortions with the changes in the atomic charges.

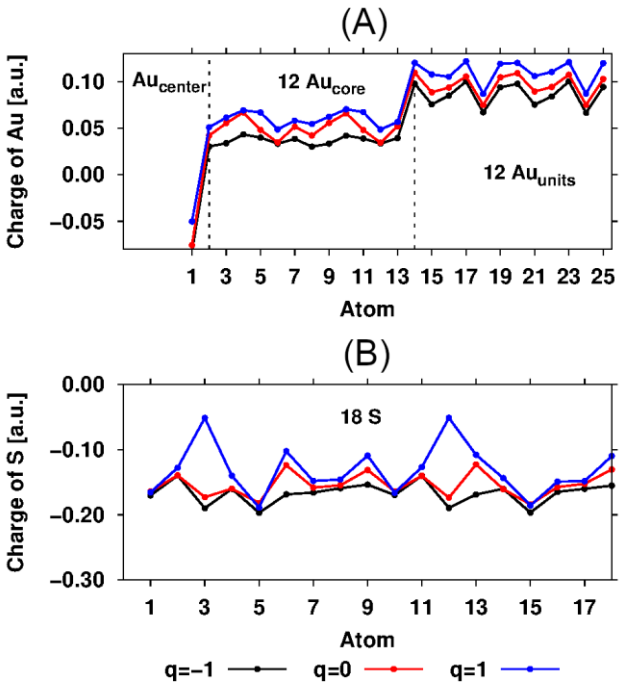

Figure 3. Atomic charges per atom type for the $[Au_{25}(SCH_2CH_2Ph)_{18}]^q$ nanoclusters (q=-1, 0, 1). The charges are calculated for (A) the central Au atom (Au_{center}), the 12 Au atoms forming the Au_{12} core (Au_{core}), the 12 Au of the units (Au_{units}), and (B) the 18 S atoms of the units.

Also, we analyzed the changes in the energy of frontier molecular orbitals of the $[Au_{25}(SCH_2CH_2Ph)_{18}]^q$ nanoclusters. In an ideal, no distorted, $[Au_{25}(SR)_{18}]^q$ nanocluster the three highest occupied molecular orbitals (HOMO, HOMO-1, and HOMO-2) and the five lowest unoccupied molecular orbitals (LUMO to LUMO+4) are expected to be triply and five-fold-degenerate, respectively. However, in Figure 4 we show that the three highest occupied molecular orbitals and the five lowest unoccupied molecular orbitals of the $[Au_{25}(SCH_2CH_2Ph)_{18}]^q$ nanoclusters are not degenerate. We observed that upon electron loss the electronic structure undergoes important modifications, such as a significant decrease of the HOMO-LUMO gap (from 1.14 eV, to 1.11 eV, to 0.41 eV when going from the anionic to neutral to the cationic cluster). In addition, we noticed that the odd number of electrons of $[Au_{25}(SCH_2CH_2Ph)_{18}]^0$ causes the destabilization of the single-electron occupied molecular orbital (labeled as HOMO*), increasing its energy by ≈ 0.14 eV above the HOMO*-1 (*i.e.* ≈0.05 eV more than in the case of the anionic cluster). Interestingly, the ground state energy of the HOMO* of the neutral cluster matches the energy of the Fermi level (E_F) (see energy diagram in Figure 4 and density of states of Figure 6B), which is used as energy reference to plot the energy diagram.

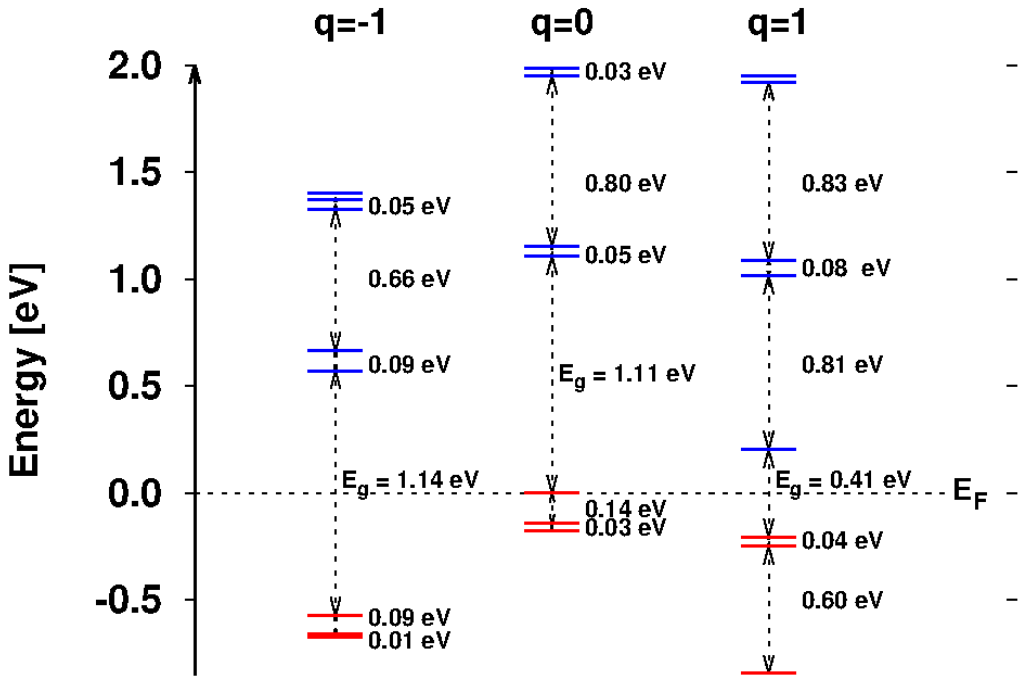

Figure 4. Energy diagram of the frontier molecular orbitals of the $[Au_{25}(SCH_2CH_2Ph)_{18}]^q$ nanoclusters (q=-1, 0, and 1). HOMO-2, HOMO-1, and HOMO are shown in red, and LUMO to LUMO+4 are in blue. The energy gap between HOMO-2-HOMO-1, HOMO-1-HOMO, HOMO-LUMO (E_g), LUMO-LUMO+1, LUMO+1-LUMO+2, and LUMO+2-LUMO+3 are indicated for each nanocluster. The energies of the molecular orbitals have been shifted by the corresponding nanocluster Fermi energy values: -1.738 eV (q=-1), -4.173 eV (q=0), and -6.031 eV (q=1). The energy of the single-electron occupied molecular orbital of the $[Au_{25}(SCH_2CH_2Ph)_{18}]^0$ nanoclusters (indicated as HOMO* in the text) lies exactly at its the Fermi level (E_F).

We now turn our focus to analyze in detail the main differences in the absorption spectra of the $[Au_{25}(SCH_2CH_2Ph)_{18}]^q$ nanoclusters and characterize the main peaks through the type of electronic transitions involved at a given energy (Figure 5). The characterization of the main absorption peaks can aid the experimental identification of the nanocluster charge state, which is of special interest during catalytic reaction experiments assisted by $[Au_{25}(SR)_{18}]^q$ clusters at aerobic conditions[36-42]. As major characteristics, the spectrum of the anionic $[Au_{25}(SCH_2CH_2Ph)_{18}]^{1-}$ nanocluster shows three main absorption peaks (labeled as α, β, and γ) and two shoulders (β', and γ'). The α peak (at 1.2 eV) is mainly determined by the HOMO→LUMO electronic transitions, whereas the β (1.4 eV) and γ (2.1 eV) peaks are governed by the transitions between HOMO/HOMO-1/HOMO-2 to LUMO/LUMO+1 (β), and HOMO-7/HOMO-6/HOMO-5 to LUMO/LUMO+1 (γ) (see Table 1 and Table S3 for more details). The absorption shoulders β', and γ' (at 1.5 eV and 2.0 eV, respectively) are determined by transitions between HOMO-2→LUMO+1 (β'), and HOMO→LUMO+2/LUMO+3/LUMO+4 (γ') (see Figure 5A-B, and Tables 1 and S3). In this spectrum the splitting between α and β peaks is 0.2 eV. Jiang, *et al*. have reported that including the spin-orbit coupling in PBE/TDDFT calculations is crucial

to observe the splitting between the HOMO→LUMO (α) and HOMO-1/HOMO-2→LUMO (β) electronic transitions[25]. Here, we demonstrate that, even though the oscillator strength related to the HOMO → LUMO electronic transitions is relatively small, the electronic transitions associated to these α and β peaks can be easily distinguished by their energy difference, without considering spin orbit effects. Additionally, the electronic transitions involving the HOMO→LUMO of $Au_{25}(SR)_{18}$ nanoclusters have been determined experimentally to occur at 1.67 eV[43, 44]. Acknowledging that the PBE functional systematically underestimates the electronic transitions by about 0.4-0.5 eV[25, 45], our calculations fall very close to the energy for the HOMO→LUMO electronic transitions that have been experimentally reported. Other theoretical studies using the PBE functional have calculated the electronic transitions between HOMO→LUMO to occur also at 1.2 eV[25, 27].

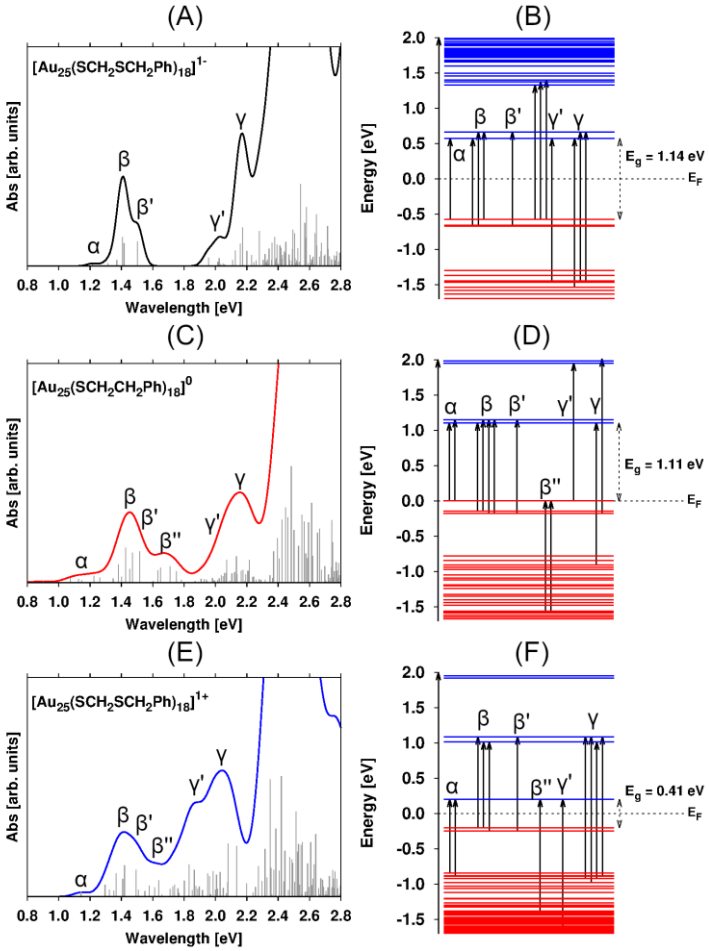

Figure 5. Absorption spectrum of (A) $[Au_{25}(SCH_2CH_2Ph)_{18}]^{1-}$, (C) $[Au_{25}(SCH_2CH_2Ph)_{18}]^{0}$ and (E) $[Au_{25}(SCH_2CH_2Ph)_{18}]^{1+}$ nanoclusters along with their corresponding (B, D, and F) energy diagram of frontier molecular orbitals. In (A, C, and E), the vertical gray lines correspond to the single oscillator strengths relative to individual electronic transitions. In (B, D, and F), the occupied and unoccupied molecular orbitals are drawn in red and blue, respectively. Some of the main electronic transitions contributing to the main absorption peaks (labeled as α, β, β', β'', γ', and γ) are depicted in the energy diagrams. The HOMO-LUMO energy gap (E_g) is indicated for each nanocluster.

Table 1. Electronic transitions contributing to the main absorption peaks (α, β, β', β'' γ', and γ) in the spectra of the $[Au_{25}(SCH_2CH_2Ph)_{18}]^q$ nanoclusters (q=-1,0, and 1). Energy peaks are in eV.

Peak (Energy)	**$[Au_{25}(SCH_2CH_2Ph)_{18}]^{1-}$**	**Peak (Energy)**	**$[Au_{25}(SCH_2CH_2Ph)_{18}]^{0}$**	**Peak (Energy)**	**$[Au_{25}(SCH_2CH_2Ph)_{18}]^{1+}$**
α (1.2)	HOMO→LUMO	α (1.1-1.2)	HOMO*→LUMO HOMO*→LUMO+1	α (1.1)	HOMO-2→LUMO HOMO-4→LUMO
β (1.4)	HOMO-1→LUMO+1 HOMO-1→LUMO HOMO→LUMO+1 HOMO-2→LUMO	β (1.4)	HOMO*-1→LUMO HOMO*-1→LUMO+1 HOMO*-2→LUMO HOMO*-2→LUMO+1	β (1.4)	HOMO→LUMO+2 HOMO→LUMO+1 HOMO-1→LUMO+1
β' (1.5)	HOMO-2→LUMO+1	β' (1.4)	HOMO*-2→LUMO+1	β' (1.5)	HOMO-1→LUMO+2
β''	---	β'' (1.7)	HOMO*-19→HOMO* HOMO*-22→HOMO*	β'' (1.6)	HOMO-18→LUMO
γ' (2.0)	HOMO→LUMO+2 HOMO→LUMO+3 HOMO→LUMO+4 HOMO-5→LUMO	γ' (1.9)	HOMO*→LUMO+2	γ' (1.8)	HOMO-36→LUMO
γ (2.1)	HOMO-7→LUMO HOMO-6→LUMO+1 HOMO-5→LUMO+1	γ (2.1)	HOMO*-5→LUMO HOMO*-2→LUMO+3	γ (2.0)	HOMO-5→LUMO+2 HOMO-6→LUMO+2 HOMO-5→LUMO+1 HOMO-4→LUMO+2

Analyzing the absorption spectrum of the neutral $[Au_{25}(SCH_2CH_2Ph)_{18}]^0$ cluster we observe that the electronic transitions between HOMO*→LUMO occur at slightly lower energy (by ≈ 0.1 eV) than in the anionic nanocluster (see Tables 1 and S4). This is a consequence of the slight reduction of the HOMO-LUMO energy gap due to the destabilization of the HOMO* in the neutral cluster. Moreover, the oscillator strength and relative contribution of HOMO*→LUMO electronic transitions to the α peak of the $[Au_{25}(SCH_2CH_2Ph)_{18}]^0$ spectrum are considerably smaller than those of the anionic nanocluster (1.94E-04, 16% vs 8.23E-04, 91%, see tables S3 and S4). Although in different reports the lowest-energy photoabsorption of the neutral cluster (labeled as α) is less evident than in the anionic one[14, 18], our calculations indicate that in the neutral nanocluster the α peak is mainly determined by the electronic transitions HOMO* → LUMO+1, HOMO*-13 →HOMO*, HOMO*-8 →HOMO*, and HOMO*-9 →HOMO* (see Table 1 and Table S4). Temperature-dependent optical measurements can potentially give more insights into the photoabsorption differences at the lowest–energy regime between the neutral and anionic nanoclusters, since some electronic excitation information may be lost when measuring the spectrum at room temperature[43]. Furthermore, the β absorption peak of the neutral cluster is mainly determined by the transitions between HOMO*-1/HOMO*-2→LUMO/LUMO+1. A difference from the anionic cluster is that the electronic transitions HOMO*-2→LUMO+1 that form the absorption shoulder β' (1.5 eV) in the spectrum of the $[Au_{25}(SCH_2CH_2Ph)_{18}]^{1-}$ cluster, they appear at slightly lower energy (≈ 1.4 eV) in the neutral nanocluster and there is no absorption shoulder (see Figures 5C-D and table 1). In the spectrum of the neutral nanocluster the γ' (1.9 eV) and γ (2.1 eV) peaks are largely determined by electronic transitions between HOMO*→LUMO+2 (γ'), HOMO*-5→LUMO, HOMO*-2→LUMO+3 (γ'), as well as by electronic transitions occurring

between low-energy occupied molecular orbitals and the HOMO* (see Table S4). An important observation in the spectrum of the $[Au_{25}(SCH_2CH_2Ph)_{18}]^0$ when compared to the anionic cluster is the quenching of the γ absorption peak, which has been also experimentally observed (occurring at ≈2.7 eV) as an evidence of cluster oxidation[14, 19]. In Figure S2, we compare the calculated spectra of the anionic and neutral $Au_{25}(SCH_2CH_2Ph)_{18}$ nanoclusters where we can notice the decrease in absorption intensity of the γ peak in the spectrum of $[Au_{25}(SCH_2CH_2Ph)_{18}]^0$.

Besides all the aforementioned differences between the spectrum of the anionic and neutral $Au_{25}(SCH_2CH_2Ph)_{18}$ nanoclusters, the most remarkable difference between the two spectra is the emergence of the absorption peak between 1.6-1.8 eV (labeled as β'') in the neutral cluster. This β'' peak corresponds to the distinct absorption shoulder that has been experimentally observed in the spectrum of the oxidized $[Au_{25}(SR)_{18}]^0$ nanocluster at about 2.0 eV[14, 18, 19]. According to our TDDFT calculations, this absorption peak, β'', arises mainly from electronic transitions between the low-energy occupied states (states with ground state energies in the energy window of -1.5 and -1.8 eV, see Figure 6B) and the HOMO* (see Table S4). According to the projected density of states shown in Figure 6, the main character of the molecular orbitals within the energy window of -1.5 to -1.8 eV are determined by the local Au(p,d), S(p) and C(p) states from the six $Au_2(SCH_2CH_2Ph)_3$ units (known as the ligand band states[21]). The character of the HOMO* is defined by the Au(s,p) and S(p) states. It is important to point out that although the ground state energy of the HOMO* matches the energy of the Fermi level, this molecular orbital does not necessarily has that energy in the relaxed excited state configuration. In fact, it has been reported that the energy of the HOMO of $[Au_{25}(SR)_{18}]^{1-}$ rises up by 0.22 eV upon photoexcitation[26]. Therefore, one could expect that decreasing even further the occupancy of this single-electron occupied molecular orbital (*e.g.* by photoexciting the system) would increase its energy beyond the E_F, making the electronic transitions associated to the β'' peak more likely to occur.

In the case of the $[Au_{25}(SCH_2CH_2Ph)_{18}]^{1+}$ nanocluster, two of the electrons that define the "magic" electronic configuration of the $[Au_{25}(SCH_2CH_2Ph)_{18}]^{1-}$ are lost. Thus, the energy of the original HOMO of the anionic cluster moves to higher energy so that it becomes the LUMO in the $[Au_{25}(SCH_2CH_2Ph)_{18}]^{1+}$ nanocluster. As a consequence of the shifting of the frontier molecular orbitals, the electronic transitions occurring in the spectrum of the positively charged nanocluster become remarkable distinct to the ones observed in the spectrum of the anionic and neutral nanoclusters. In the spectrum of $[Au_{25}(SCH_2CH_2Ph)_{18}]^{1+}$ shown in Figure 5E, we noticed that the oscillator strength relative to the HOMO→LUMO transitions is remarkable small (of the order of 10^{-8}), indicating the low probability of these type of transitions. Instead, the main contributions to the lowest-energy absorption peak (α) in the spectrum of $[Au_{25}(SCH_2CH_2Ph)_{18}]^{1+}$ arise from electronic transitions between HOMO-2/HOMO-4 → LUMO, and the peaks β (1.4 eV) and β' (1.5 eV) are mainly determined by the transitions between HOMO/HOMO-1→LUMO+1/LUMO+2. Similarly as in the neutral cluster, the cationic cluster displays the β'' absorption peak. However, the intensity of this β'' peak in the spectrum of $[Au_{25}(SCH_2CH_2Ph)_{18}]^{1+}$ is higher than in the neutral nanocluster. Moreover, the contributions to this β'' peak arise from electronic transitions between

low-energy molecular orbitals (orbitals with ground state energy between -1.3 eV to -1.4 eV) and the LUMO. According to the density of states shown in Figure 6C, the character of these low-energy orbitals is primarily determined by the local Au(s,p,d), S(p) and C(p) states from the $Au_2(SCH_2CH_2Ph)_3$ units, whereas the LUMO is mainly defined by the local Au(p) and S(p) states (Figure 6 C).

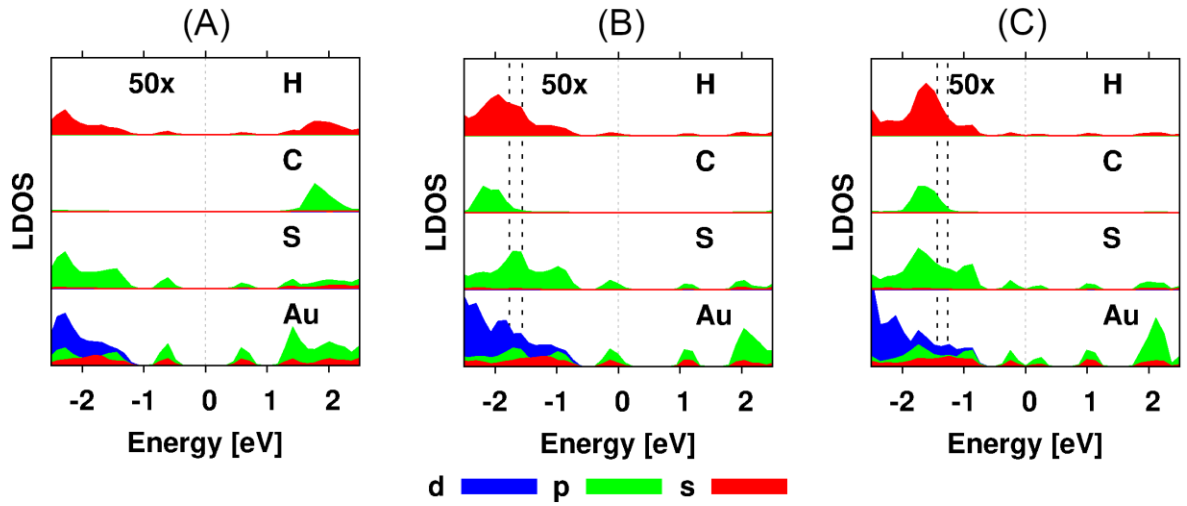

Figure 6. Local projected density of states (LPDOS) per atom type of (A) $[Au_{25}(SCH_2CH_2Ph)_{18}]^{1-}$, (B) $[Au_{25}(SCH_2CH_2Ph)_{18}]^{0}$ and (C) $[Au_{25}(SCH_2CH_2Ph)_{18}]^{1+}$ nanoclusters. The dark-dashed lines indicate the energy ranges of occupied molecular orbitals (-1.56 eV to -1.77 eV in (B) and -1.26 eV to -1.43 eV in (C)) that are contributing to the distinct absorption peaks (β'') of the $[Au_{25}(SCH_2CH_2Ph)_{18}]^{0}$ and $[Au_{25}(SCH_2CH_2Ph)_{18}]^{1+}$ spectra.

To shed light on the effect of the phenylethanethiolate ligands on the electronic structure of the $[Au_{25}(SR)_{18}]^{q}$ nanoclusters, we calculated the ground state properties and absorption spectrum of the simplified models $[Au_{25}(SCH_3)_{18}]^{1-}$ and $[Au_{25}(SH)_{18}]^{1-}$ and compared them with the properties of $[Au_{25}(SCH_2CH_2Ph)_{18}]^{1-}$. In Figure 7, we show the structure of the simplified nanoclusters, which atomic connectivity in the inorganic $Au_{25}S_{18}$ core is the same as for the $[Au_{25}(SCH_2CH_2Ph)_{18}]^{q}$ clusters described above (see Figure 1B).

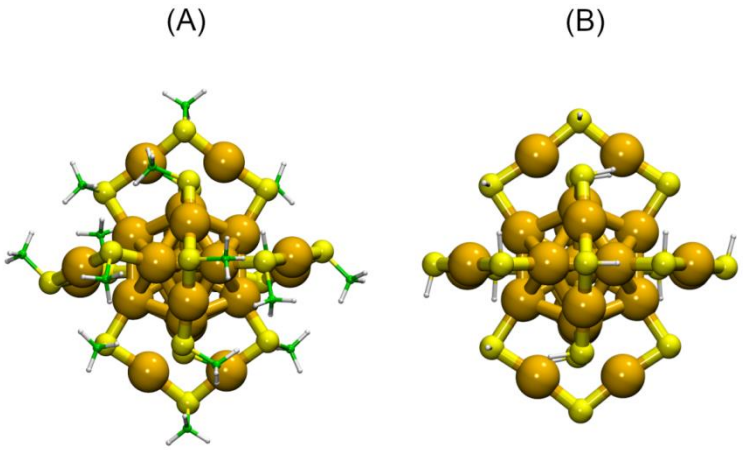

Figure 7. Atomic structure of the (A) $[Au_{25}(SCH_3)_{18}]^{1-}$ and (B) $[Au_{25}(SH)_{18}]^{1-}$ nanoclusters. Orange, yellow, green, and white spheres represent the Au, S, C, and H atoms.

Comparing of the Au-Au and Au-S bond distances of $[Au_{25}(SCH_3)_{18}]^{1-}$ and $[Au_{25}(SH)_{18}]^{1-}$ with respect to the corresponding bonds of the $[Au_{25}(SCH_2CH_2Ph)_{18}]^{1-}$ nanocluster, we found that the simplification of the true $-SCH_2CH_2Ph$ ligands by the $-SCH_3$ or -SH groups does not affect the Au_{core}-Au_{core}, Au_{core}-S and Au_{units}-S bonds (see Figure 8 B-D). Also, we found that the Au_{center}-Au_{core} bonds of the simplified structures are more uniform than in the $[Au_{25}(SCH_2CH_2Ph)_{18}]^{1-}$ nanocluster, in which two of the Au_{center}-Au_{core} bonds are slightly elongated (by less than 0.1 Å) compared to the rest Au_{center}-Au_{core} bonds (see Figure 8A).

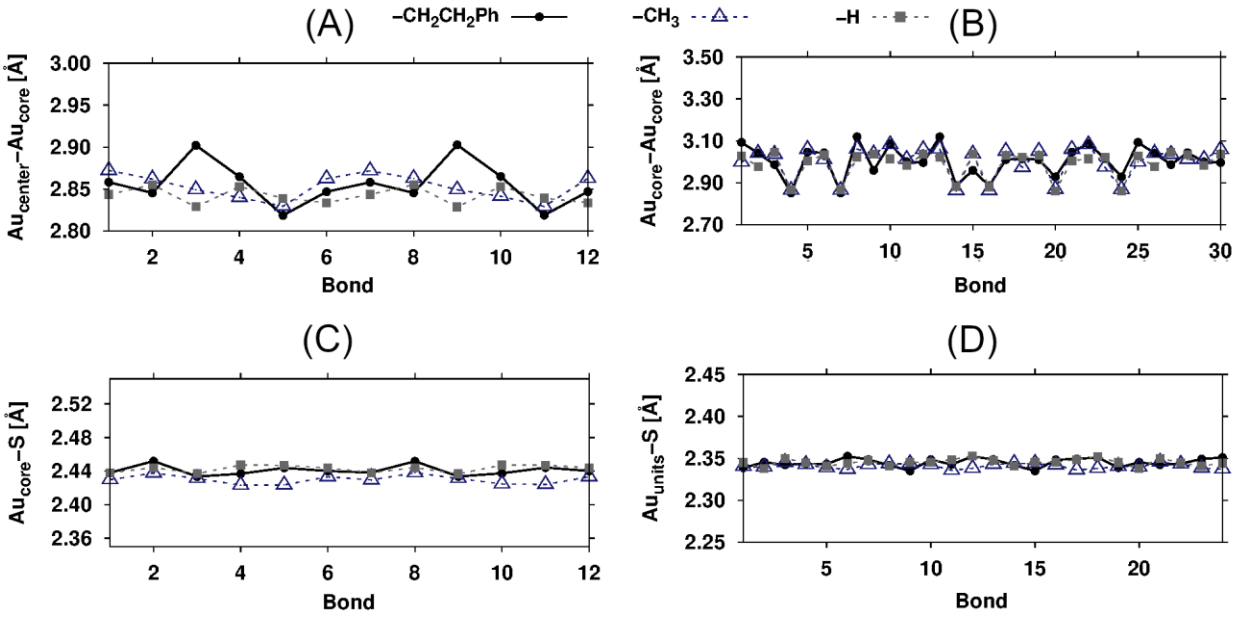

Figure 8. Individual (A) Au_{center}-Au_{core}, (B) Au_{core}-Au_{core}, (C) Au_{core}-S, and (D) Au_{units}-S bond distances of the $[Au_{25}(SR)_{18}]^{1-}$ nanoclusters. Circles (solid), triangles (dashed), and squares (dashed) indicate the bond distances in $[Au_{25}(SCH_2CH_2Ph)_{18}]^{1-}$, $[Au_{25}(SCH_3)_{18}]^{1-}$, and $[Au_{25}(SH)_{18}]^{1-}$ respectively.

Also for these simplified structures, we calculate the atomic (Bader) charges. In contrast to the $[Au_{25}(SCH_2CH_2Ph)_{18}]^q$ clusters, we found no significant changes in the atomic charges of the metal core. Only slight deviations (of up to ≈ 11%) were found in the charges of the S and Au atoms of the units of $[Au_{25}(SCH_3)_{18}]^{1-}$ with respect to the $[Au_{25}(SCH_2CH_2Ph)_{18}]^{1-}$ nanocluster (see Figure 9 B and Table S2).

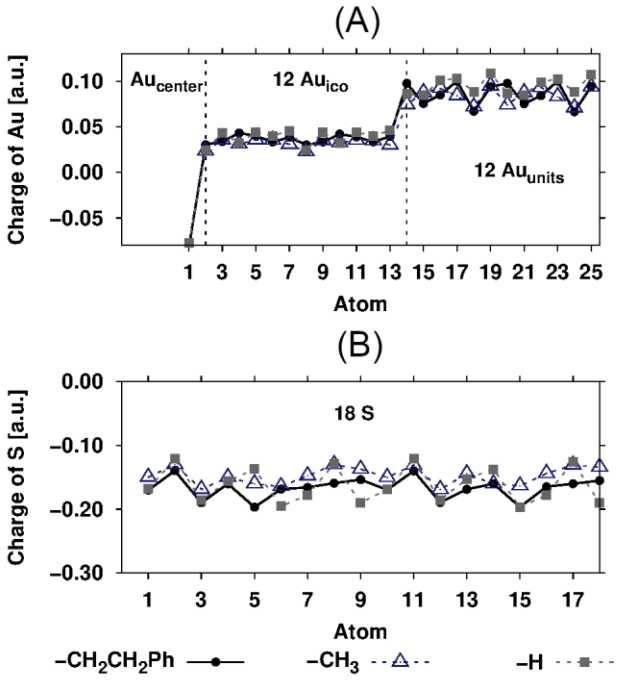

Figure 9. Atomic charges per atom type for the $[Au_{25}(SR)_{18}]^{1-}$ nanoclusters. The charges are calculated for (A) the central Au atom (Au_{center}), the 12 Au atoms forming the Au_{12} core (Au_{core}), the 12 Au atoms of the units, and (B) the 18 S atoms. Circles (solid), triangles (dashed), and squares (dashed) indicate the atomic charges of S and Au atoms in $[Au_{25}(SCH_2CH_2Ph)_{18}]^{1-}$, $[Au_{25}(SCH_3)_{18}]^{1-}$, and $[Au_{25}(SH)_{18}]^{1-}$ respectively.

Even though the Au_{center}-Au_{core} bonds of the $[Au_{25}(SCH_2CH_2Ph)_{18}]^{1-}$ nanocluster are distorted by less than ≈0.1 Å (less than 3%), these small geometric changes in Au_{13} core introduce significant modifications in the energy of the frontier molecular orbitals of the $[Au_{25}(SCH_2CH_2Ph)_{18}]^{1-}$ nanocluster. By comparing the energy of the frontier molecular orbitals of the $[Au_{25}(SCH_3)_{18}]^{1-}$ and $[Au_{25}(SH)_{18}]^{1-}$ (which have more uniform Au-Au bond lengths) with the energy of the corresponding molecular orbitals of $[Au_{25}(SCH_2CH_2Ph)_{18}]^{1-}$, we found that the full -SCH_2CH_2Ph ligands enhance the splitting of the molecular orbitals. In particular, we found that while in the $[Au_{25}(SCH_3)_{18}]^{1-}$ and $[Au_{25}(SH)_{18}]^{1-}$ nanoclusters the highest occupied molecular orbital (HOMO) and HOMO-1 and HOMO-2 are almost degenerate (with energy differences between 0.01-0.02eV), in the $[Au_{25}(SCH_2CH_2Ph)_{18}]^{1-}$ nanocluster these molecular orbitals split by ≈ 0.1 eV. Similarly, the energy separation between the lowest unoccupied molecular orbital (LUMO) and LUMO+1 is at least twice the splitting of these molecular orbitals in the simplified

nanoclusters. This suggests that the small changes in the bond distances of $[Au_{25}(SCH_2CH_2Ph)_{18}]^{1-}$ due to the presence of the actual (full) ligands, significantly change the energy of the frontier molecular orbitals by breaking the degeneracy. This ultimately can lead to significant modifications in the shape and energy of the main absorption features of the spectrum of these nanoclusters. To verify that the orbital splitting enhancement in $[Au_{25}(SCH_2CH_2Ph)_{18}]^{1-}$ is merely due to the distortions of the metal core caused by the $-SCH_2CH_2Ph$ ligands, we used the $Au_{25}S_{18}$ core structure of the $[Au_{25}(SCH_2CH_2Ph)_{18}]^{1-}$ to build a new $[Au_{25}(SH)_{18}]^{1-}$ structure in which only the H atoms were relaxed (partial optimization with the $Au_{25}S_{18}$ core being frozen). For this new $[Au_{25}(SH)_{18}]^{1-}$ structure, we found that the splitting of the frontier molecular is similar to the one of $[Au_{25}(SCH_2CH_2Ph)_{18}]^{1-}$, which confirms that the enhancement of orbital splitting is merely due to the small distortions introduced by the phenylethanethiolate ligands in the metal core of $[Au_{25}(SCH_2CH_2Ph)_{18}]^{1-}$ (see Figure S7).

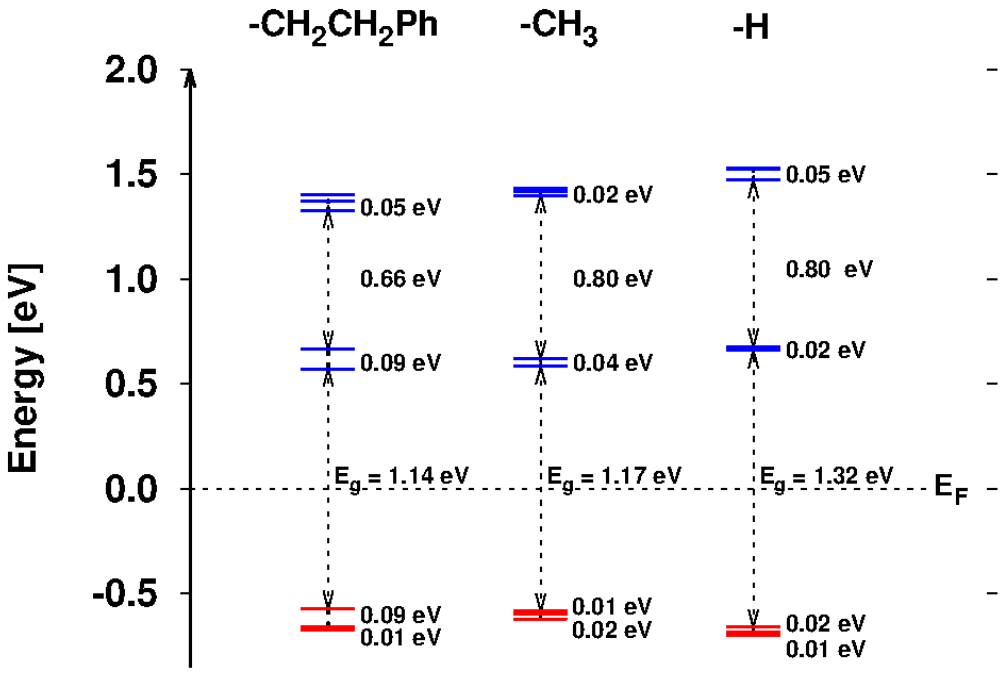

Figure 10. Energy of the frontier molecular orbitals of the $[Au_{25}(SR)_{18}]^{1-}$ nanoclusters (R = $-CH_2CH_2Ph$, $-CH_3$ or –H). HOMO-2, HOMO-1, and HOMO are shown in red, and LUMO to LUMO+4 are in blue. The energy gap between HOMO-2-HOMO-1, HOMO-1-HOMO, HOMO-LUMO (E_g), LUMO-LUMO+1, LUMO+1-LUMO+2, and LUMO+2-LUMO+3 are indicated for each nanocluster. The energies of the molecular orbitals have been shifted by the corresponding nanocluster Fermi energy value: -1.738 eV (R=$-CH_2CH_2Ph$), -1.439 eV (R=$-CH_3$), and -1.864 eV (R=-H).

Furthermore, we analyze the absorption spectra of the simplified $[Au_{25}(SCH_3)_{18}]^{1-}$ and $[Au_{25}(SH)_{18}]^{1-}$ clusters and compare them with respect to the spectrum of $[Au_{25}(SCH_2CH_2Ph)_{18}]^{1-}$

(Figure 11). According to the "superatom" theory, the main absorption peaks in the low-energy regime of the optical spectrum of $[Au_{25}(SR)_{18}]^{1-}$ are primarily dominated by the metal-to-metal transitions[13, 46]. Therefore, one would expect the absorption spectrum of the $[Au_{25}(SCH_2CH_2Ph)_{18}]^{1-}$, $[Au_{25}(SCH_3)_{18}]^{1-}$, and $[Au_{25}(SH)_{18}]^{1-}$ nanocluster to look very similar. However, we found that the spectra of the simplified structures display more defined α, β, and γ absorption peaks (and a small shoulder, γ', in the case of $[Au_{25}(SCH_3)_{18}]^{1-}$) as consequence of the lack of actual full ligands. Moreover, in the case of $[Au_{25}(SH)_{18}]^{1-}$ the three main absorption peaks are systematically blue-shifted by ≈0.2 eV with respect to the corresponding peaks of $[Au_{25}(SCH_2CH_2Ph)_{18}]^{1-}$. In addition, the HOMO→ LUMO transitions, which in the spectrum of $Au_{25}(SCH_2CH_2Ph)_{18}]^{1-}$ occurs at 1.2 eV, in the spectra of the simplified $[Au_{25}(SCH_3)_{18}]^{1-}$ and $[Au_{25}(SH)_{18}]^{1-}$ models occur at ≈1.3 eV and ≈1.4 eV, respectively. Also, as a consequence of the small splitting between the frontier molecular orbitals, the α peak of the spectrum of the $[Au_{25}(SCH_3)_{18}]^{1-}$, and $[Au_{25}(SH)_{18}]^{1-}$ nanocluster is formed by many other electronic transitions besides HOMO→LUMO, such as HOMO-1→LUMO/LUMO+1 and HOMO-2→LUMO. Furthermore, the main transitions contributing to the higher-energy peaks, β and γ, of the simplified nanoclusters are also different from the ones observed in $[Au_{25}(SCH_2CH_2Ph)_{18}]^{1-}$ (see Figure 11 and Tables 2 and S5). Moreover, in the spectra of the simplified nanoclusters the β' shoulder (characterized by the electronic transition HOMO-2→LUMO+1) disappears. These results suggest that introducing small distortion (of ≈ 0.1 Å), *e.g.* by modifying the nature of the organothiolate molecules, can affect the energy of the frontier molecular orbitals leading to the broadening of the low-energy absorption peaks and, in some cases, to the emergence of absorption shoulders. The direct comparison between the spectrum of the $[Au_{25}(SCH_2CH_2Ph)_{18}]^{1-}$ and the spectra of the simplified nanoclusters is shown in Figure S5. In addition, we also calculated the spectrum of the $[Au_{25}(SCH_3)_{18}]^{q}$ nanoclusters (with q=-1, 0, and 1) and plotted their molecular orbital energies (Figures S3 and S4). By comparing the molecular orbital diagrams of the $[Au_{25}(SCH_3)_{18}]^{q}$ with the $[Au_{25}(SCH_2CH_2Ph)_{18}]^{q}$ nanoclusters at each oxidation state, we observe that while the effect of the $-SCH_2CH_2Ph$ ligands to enhance the energy splitting of the frontier molecular orbitals is pronounced for the neutral and anionic nanoclusters, it is less marked in the cationic nanocluster (see Figures 4 and S4). However, similar to the phenylethanethiolate-protected nanoclusters, in the $[Au_{25}(SCH_3)_{18}]^{q}$ nanoclusters we observe the destabilization of the frontier molecular orbitals due to electron loss (Figure S4) and the development of additional absorption features at 1.6-1.8 eV with increasing oxidation state (Figure S3).Thus, our findings highlight that simplification of the actual experimental ligands comprising the nanocluster with smaller organic groups to reduce computational cost, modify the optical features resulting to deviations from experiments. In addition, our calculations demonstrate that bulkier ligands can induce distortions in the core of the nanocluster due to an induced strain that emanates from ligand-ligand interactions on the surface, affecting the electronic transitions and optical features of the nanocluster.

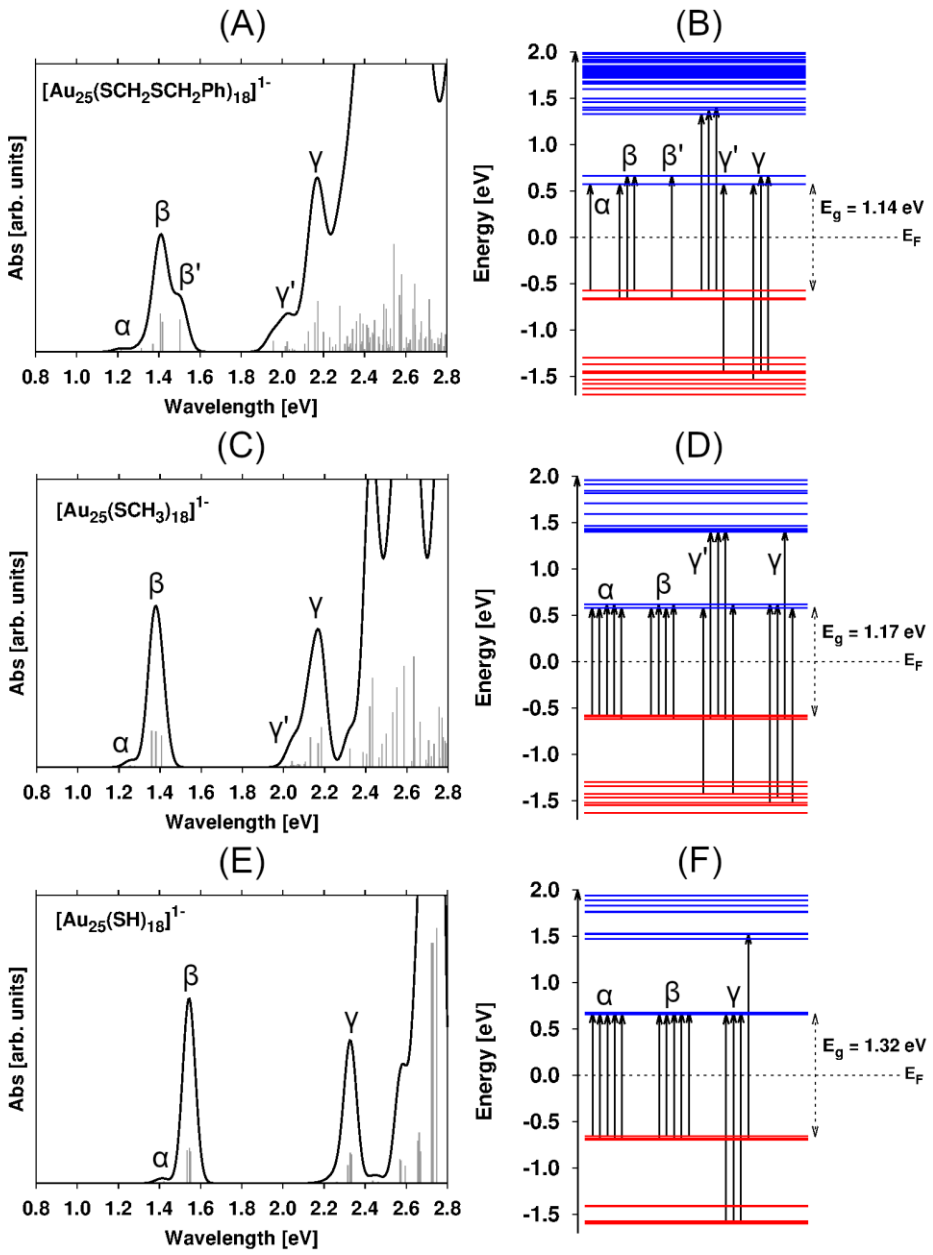

Figure 11. Absorption spectrum of (A) $[Au_{25}(SCH_2CH_2Ph)_{18}]^{1-}$, (C) $[Au_{25}(SCH_3)_{18}]^{1-}$ and (E) $[Au_{25}(SH)_{18}]^{1-}$ nanoclusters along with their corresponding energy diagram of frontier molecular orbitals (B, D, and F). In (A), (C), and (E), the vertical gray lines correspond to the single oscillator strengths relative to individual electronic transitions. In (B) , (D), and (F) the occupied and unoccupied molecular orbitals are drawn in red and blue, respectively. Some of the main electronic transitions contributing to the main absorption peaks (labeled as α, β, γ', and γ) are depicted in the energy diagrams. The HOMO-LUMO energy gap (E_g) is indicated for each nanocluster.

Table 2. Electronic transitions contributing to the main absorption peaks (α, β, β', γ', and γ) in the spectra of the $[Au_{25}(SR)_{18}]^{1-}$ nanoclusters (R = $-CH_2CH_2Ph$, $-CH_3$, –H). Energy peaks are in eV.

Peak (Energy)	**$[Au_{25}(SCH_2CH_2Ph)_{18}]^{1-}$**	**Peak (Energy)**	**$[Au_{25}(SCH_3)_{18}]^{1-}$**	**Peak (Energy)**	**$[Au_{25}(SH)_{18}]^{1-}$**
α (1.2)	HOMO→LUMO	α (1.3)	HOMO→LUMO HOMO-1→LUMO HOMO-1→LUMO+1 HOMO→ LUMO+1 HOMO-2→LUMO	α (1.4)	HOMO→LUMO HOMO→LUMO+1 HOMO-1→LUMO HOMO-2→LUMO+1 HOMO-2→LUMO
β (1.4)	HOMO-1→LUMO+1 HOMO-1→LUMO HOMO→LUMO+1	β (1.4)	HOMO→LUMO HOMO-1→LUMO HOMO-2→LUMO+1 HOMO→LUMO+1 HOMO-2→LUMO HOMO-1→LUMO+1	β (1.5)	HOMO→LUMO HOMO-2→LUMO HOMO-1→LUMO+1 HOMO-2→LUMO+1 HOMO→LUMO+1
β' (1.5)	HOMO-2→LUMO+1	β'	---	β'	----
γ' (2.0)	HOMO→LUMO+2 HOMO→LUMO+3 HOMO→LUMO+4 HOMO-5→LUMO	γ' (2.0)	HOMO-5→LUMO HOMO-2→LUMO+2 HOMO-1→LUMO+2 HOMO-2→LUMO+3 HOMO-5→LUMO+1	γ'	----
γ (2.1)	HOMO-7→LUMO HOMO-6→LUMO+1 HOMO-5→LUMO+1	γ (2.1)	HOMO-7→LUMO+1 HOMO-2→LUMO+3 HOMO-7→LUMO HOMO-6→LUMO+1	γ (2.3)	HOMO-7→LUMO HOMO-6→LUMO+1 HOMO-5→LUMO+1 HOMO-1→LUMO+3

Conclusions

In summary, we have employed first principles calculations and demonstrated that the conversion of $[Au_{25}(SR)_{18}]^{1-}$ into $[Au_{25}(SR)_{18}]^{0}$ or $[Au_{25}(SR)_{18}]^{1+}$ is accompanied by significant modifications in the molecular and electronic structure of the nanoclusters. In particular, we have demonstrated that, relative to the anionic cluster, the oxidized $[Au_{25}(SR)_{18}]^{0}$ and $[Au_{25}(SR)_{18}]^{1+}$ structures elongate the Au-Au bonds (by 5-14%), and the Au-S bonds shrink (by less than 2%). Also we demonstrated that as the charge state of the nanocluster increases, the Au_{25} core become more positive and the S atoms withdraw less electron density from the metal core. Moreover, upon oxidation the energy of the frontier molecular orbitals undergoes significantly modifications that lead to different HOMO-LUMO band gaps and distinct density of states. All these geometric and electronic structural changes due to the charge state manifest in the absorption spectra of the $[Au_{25}(SR)_{18}]^{0/1+}$ nanoclusters by the emergence of additional absorption features ≈1.6-1.8 eV (observed experimentally at ≈2.0 eV). We demonstrated that these distinctive peaks in the spectra of the oxidized clusters arise mainly from electronic transitions involving low-energy molecular orbitals from the staple motifs.

Furthermore, we analyzed the effect of ligands on the structure and absorption spectrum of $[Au_{25}(SR)_{18}]^{1-}$. By replacing the actual, experimentally used $-SCH_2CH_2Ph$ ligands with the -SH or

-SCH_3 groups, we demonstrated that the phenylethanethiolate groups introduce small changes in the length of the Au-Au bonds of the Au_{13} kernel. Interesting enough, these small structural changes are sufficient to cause a splitting in the frontier molecular orbitals (by ≈ 0.1 eV), which ultimately reflects in the absorption spectra by the broadening of the absorption peaks (and/or the development of absorption shoulders) associated with the metal-to-metal transitions. Moreover, the energy of the main absorption peaks can be significantly blue-shifted when using the simple -SH as model ligands. Thus, the detailed characterization of the main absorption peaks in the spectrum of the $[Au_{25}(SR)_{18}]^q$ nanoclusters carried out in this work, provides valuable information to determine the effect of protecting ligands on the electronic structure of the nanoclusters. In addition to demonstrating an agreement between our calculations and experiments, our work has a twofold contribution: it aids the experimental determination of the nanocluster charge state and demonstrates deviations in the calculation of optical spectra originating from the choice of model ligands on the nanoclusters.

Acknowledgements

The support of the U.S. Department of Energy, National Energy Technology Laboratory through NETL-Penn State University Coalition for Fossil Energy Research (UCFER, contract number DE-FE0026825) is gratefully acknowledged. The authors would like to acknowledge computational support from the Center for Research Computing at the University of Pittsburgh and the Extreme Science and Engineering Discovery Environment, which is supported by the NSF (ACI-1548562).

Conflicts of interest

There are no conflicts of interest to declare.

Corresponding author

*e-mail: gmpourmp@pitt.edu

References

1. I. Chakraborty and T. Pradeep, *Chem. Rev.*, 2017, **117**, 8208-8271.
2. R. Jin, C. Zeng, M. Zhou and Y. Chen, *Chem. Rev.*, 2016, **116**, 10346-10413.
3. T. Tsukuda and H. Häkkinen , *Protected Metal Clusters: From Fundamentals to Applications*, Elsevier, Amsterdam, 2015.
4. Q. Li, T.-Y. Luo, M. G. Taylor, S. Wang, X. Zhu, Y. Song, G. Mpourmpakis, N. L. Rosi and R. Jin, *Sci. Adv.*, 2017, **3**, e1603193.
5. J. Akola, M. Walter, R. L. Whetten, H. Häkkinen and H. Grönbeck, *J. Am. Chem. Soc.*, 2008, **130**, 3756-3757.
6. M. G. Taylor and G. Mpourmpakis, *Nat. Commun.*, 2017, **8**, 15988.
7. S. Zhao, N. Austin, M. Li, Y. Song, S. D. House, S. Bernhard, J. C. Yang, G. Mpourmpakis and R. Jin, *ACS Catal*, 2018, **8**, 4996-5001.

8. M. W. Heaven, A. Dass, P. S. White, K. M. Holt and R. W. Murray, *J. Am. Chem. Soc.*, 2008, **130**, 3754-3755.
9. M. Zhu, C. M. Aikens, F. J. Hollander, G. C. Schatz and R. Jin, *J. Am. Chem. Soc.*, 2008, **130**, 5883-5885.
10. X. Kang, H. Chong and M. Zhu, *Nanoscale*, 2018, **10**, 10758-10834.
11. J. F. Parker, C. A. Fields-Zinna and R. W. Murray, *Acc. Chem. Res.*, 2010, **43**, 1289-1296.
12. W. A. de Heer, *Rev. Mod. Phys.*, 1993, **65**, 611-676.
13. M. Walter, J. Akola, O. Lopez-Acevedo, P. D. Jadzinsky, G. Calero, C. J. Ackerson, R. L. Whetten, H. Grönbeck and H. Häkkinen, *Pro. Natl. Acad. Sci.*, 2008, **105**, 9157.
14. M. Zhu, W. T. Eckenhoff, T. Pintauer and R. Jin, *J. Phys. Chem. C*, 2008, **112**, 14221-14224.
15. Y. Negishi, N. K. Chaki, Y. Shichibu, R. L. Whetten and T. Tsukuda, *J. Am. Chem. Soc.*, 2007, **129**, 11322-11323.
16. M. A. Tofanelli, K. Salorinne, T. W. Ni, S. Malola, B. Newell, B. Phillips, H. Häkkinen and C. J. Ackerson, *Chem. Sci.*, 2016, **7**, 1882-1890.
17. A. Venzo, S. Antonello, J. A. Gascón, I. Guryanov, R. D. Leapman, N. V. Perera, A. Sousa, M. Zamuner, A. Zanella and F. Maran, *Anal. Chem.*, 2011, **83**, 6355-6362.
18. S. Bhat, R. P. Narayanan, A. Baksi, P. Chakraborty, G. Paramasivam, R. R. J. Methikkalam, A. Nag, G. Natarajan and T. Pradeep, *J. Phys. Chem. C*, 2018, **122**, 19455-19462.
19. D. R. Kauffman, D. Alfonso, C. Matranga, G. Li and R. Jin, *J. Phys. Chem. Lett.*, 2013, **4**, 195-202.
20. J. Enkovaara, C. Rostgaard, J. J. Mortensen, J. Chen, M. Dułak, L. Ferrighi, J. Gavnholt, C. Glinsvad, V. Haikola, H. A. Hansen, H. H. Kristoffersen, M. Kuisma, A. H. Larsen, L. Lehtovaara, M. Ljungberg, O. Lopez-Acevedo, P. G. Moses, J. Ojanen, T. Olsen, V. Petzold, N. A. Romero, J. Stausholm-Møller, M. Strange, G. A. Tritsaris, M. Vanin, M. Walter, B. Hammer, H. Häkkinen, G. K. H. Madsen, R. M. Nieminen, J. K. Nørskov, M. Puska, T. T. Rantala, J. Schiøtz, K. S. Thygesen and K. W. Jacobsen, *J. Phys.: Condens. Matter*, 2010, **22**, 253202.
21. C. M. Aikens, *J. Phys. Chem. Lett.*, 2011, **2**, 99-104.
22. S. Antonello, N. V. Perera, M. Ruzzi, J. A. Gascón and F. Maran, *J. Am. Chem. Soc.*, 2013, **135**, 15585-15594.
23. C. M. Aikens, *J. Phys. Chem. C*, 2008, **112**, 19797-19800.
24. C. M. Aikens, *J. Phys. Chem. A*, 2009, **113**, 10811-10817.
25. D.-e. Jiang, M. Kühn, Q. Tang and F. Weigend, *J. Phys. Chem. Lett.*, 2014, **5**, 3286-3289.
26. K. L. D. M. Weerawardene and C. M. Aikens, *J. Am. Chem. Soc.*, 2016, **138**, 11202-11210.
27. R. D. Senanayake, A. V. Akimov and C. M. Aikens, *J. Phys. Chem. C*, 2017, **121**, 10653-10662.
28. T. G. Schaaff and R. L. Whetten, *J. Phys. Chem. B*, 2000, **104**, 2630-2641.
29. R. L. Donkers, Y. Song and R. W. Murray, *Langmuir*, 2004, **20**, 4703-4707.
30. R. Guo and R. W. Murray, *J. Am. Chem. Soc.*, 2005, **127**, 12140-12143.
31. A. Tlahuice-Flores, R. L. Whetten and M. Jose-Yacaman, *J. Phys. Chem. C*, 2013, **117**, 20867-20875.
32. J. P. Perdew, K. Burke and M. Ernzerhof, *Phys. Rev. Lett.*, 1996, **77**, 3865-3868.
33. J. J. Mortensen, L. B. Hansen and K. W. Jacobsen, *Phys. Rev. B*, 2005, **71**, 035109.
34. G. Henkelman, A. Arnaldsson and H. Jónsson, *Comput. Mater. Sci.*, 2006, **36**, 354-360.
35. J. Akola, K. A. Kacprzak, O. Lopez-Acevedo, M. Walter, H. Grönbeck and H. Häkkinen, *J. Phys. Chem. C*, 2010, **114**, 15986-15994.
36. Y. Liu, H. Tsunoyama, T. Akita, S. Xie and T. Tsukuda, *ACS Catalysis*, 2011, **1**, 2-6.
37. X. Zhao and D. Liu, *Bioenergy Res.*, 2013, **6**, 436-447.
38. X. Nie, H. Qian, Q. Ge, H. Xu and R. Jin, *ACS Nano*, 2012, **6**, 6014-6022.
39. S. Xie, H. Tsunoyama, W. Kurashige, Y. Negishi and T. Tsukuda, *ACS Catalysis*, 2012, **2**, 1519-1523.
40. S. Yamazoe, K. Koyasu and T. Tsukuda, *Acc. Chem. Res.*, 2014, **47**, 816-824.
41. T. A. Dreier, O. Andrea Wong and C. J. Ackerson, *Chem. Commun.*, 2015, **51**, 1240-1243.

42. Y. Zhu, H. Qian, M. Zhu and R. Jin, *Adv. Mater.*, 2010, **22**, 1915-1920.
43. M. S. Devadas, S. Bairu, H. Qian, E. Sinn, R. Jin and G. Ramakrishna, *J. Phys. Chem. Lett.*, 2011, **2**, 2752-2758.
44. D. Lee, R. L. Donkers, G. Wang, A. S. Harper and R. W. Murray, *J. Am. Chem. Soc.*, 2004, **126**, 6193-6199.
45. M. J. Alhilaly, M. S. Bootharaju, C. P. Joshi, T. M. Besong, A.-H. Emwas, R. Juarez-Mosqueda, S. Kaappa, S. Malola, K. Adil, A. Shkurenko, H. Häkkinen, M. Eddaoudi and O. M. Bakr, *J. Am. Chem. Soc.*, 2016, **138**, 14727-14732.
46. C. M. Aikens, *Acc. Chem. Res.*, 2018, **51**, 3065-3073.

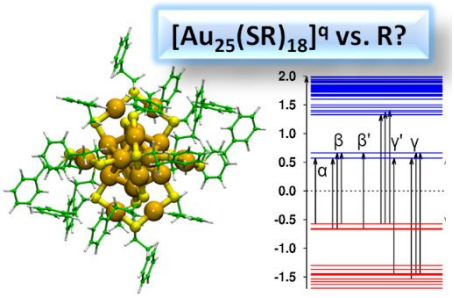

Density Functional Theory calculations reveal how optical spectra of $[Au_{25}(SR)_{18}]^q$ nanoclusters (q=-1, 0, +1) change with different ligands.